Check for updates

JGR Space Physics

RESEARCH ARTICLE
10.1029/2021JA029330

Fine Structure of Chorus Wave Packets: Comparison Between Observations and Wave Generation Models

X.-J. Zhang[1], A. G. Demekhov[2,3], Y. Katoh[4], D. Nunn[5], X. Tao[6,7,8], D. Mourenas[9], Y. Omura[10], A. V. Artemyev[1,11], and V. Angelopoulos[1]

[1]Department of Earth, Planetary, and Space Sciences, University of California, Los Angeles, Los Angeles, CA, USA, [2]Polar Geophysical Institute, Apatity, Russia, [3]Institute of Applied Physics, RAS, Nizhny Novgorod, Russia, [4]Department of Geophysics, Graduate School of Science, Tohoku University, Sendai, Japan, [5]School of Electronics and Computer Science, Southampton University, Southampton, UK, [6]CAS Key Laboratory of Geospace Environment, Department of Geophysics and Planetary Sciences, University of Science and Technology of China, Hefei, China, [7]CAS Center for Excellence in Comparative Planetology, Hefei, China, [8]Mengcheng National Geophysical Observatory, University of Science and Technology of China, Hefei, China, [9]Laboratoire Matière en Conditions Extrêmes, Paris-Saclay University, CEA, Bruyères-le-Châtel, France, [10]Research Institute for Sustainable Humanospher, Kyoto University, Kyoto, Japan, [11]Space Research Institute of Russian Academy of Sciences, Moscow, Russia

Key Points:

- Four different codes of chorus wave nonlinear generation well reproduce the observed wave packet characteristics
- The simulations recover complementary domains of observed wave packets sizes, amplitudes, and frequency sweep rates
- The simulations reproduce the observed short wave packets with high positive and negative frequency sweep rates

Correspondence to:
X.-J. Zhang,
xjzhang@ucla.edu

Citation:
Zhang, X.-J., Demekhov, A. G., Katoh, Y., Nunn, D., Tao, X., Mourenas, D., et al. (2021). Fine structure of chorus wave packets: Comparison between observations and wave generation models. *Journal of Geophysical Research: Space Physics*, *126*, e2021JA029330. https://doi.org/10.1029/2021JA029330

Received 10 MAR 2021
Accepted 28 JUL 2021

Abstract Intense lower band chorus waves are ubiquitous in the inner magnetosphere. Their properties have been modeled by various codes and investigated using measurements of many spacecraft missions. This study aims to compare simulated and observed properties of chorus waves. We present detailed comparisons between results from four different codes of nonlinear chorus wave generation and statistical observations from satellites, focusing on the fine structure of such chorus waves. We show that simulations performed with these different codes well reproduce the observed wave packet characteristics, although in somewhat complementary parameter domains as concerns wave packets sizes, amplitudes, and frequency sweep rates. In particular, simulations generate both the frequently observed short wave packets with high positive and negative frequency sweep rates, and the more rare long and intense packets with mainly rising tones. Moreover, simulations reproduce quantitatively both the increase of the size of the observed chorus wave packets with their peak amplitude, and the fast decrease of their frequency sweep rate as their size increases. This confirms the reliability of the main existing codes for accurately modeling chorus wave generation, although we find that initial conditions should be carefully selected to reproduce a given parameter range.

1. Introduction

Chorus waves are among the most intense and ubiquitous electromagnetic waves present in the inner magnetosphere (Agapitov et al., 2013; Cattell et al., 2008; Cully et al., 2011; Li, Bortnik, et al., 2011; Meredith et al., 2001; Tsurutani & Smith, 1974). They are most intense in the lower band frequency range between $0.1f_{ce}$ and $0.5f_{ce}$ (with f_{ce} the equatorial gyrofrequency), where they mainly propagate with low wave normal angles (Agapitov et al., 2013; Agapitov, Mourenas, et al., 2018; Li et al., 2013; Santolík, Macúšová, et al., 2014) under the form of rising tones (Cully et al., 2011; Li, Thorne, et al., 2011; Macúšová et al., 2010) typically lasting ~100 – 300 ms. Their linear excitation in the equatorial region by injected anisotropic electrons (LeDocq et al., 1998; Santolík et al., 2004) and their nonlinear growth under the form of rising tones have been well reproduced by various particle-in-cell codes, Vlasov hybrid codes, and semi-analytical models (Demekhov et al., 2017; Demekhov & Trakhtengerts, 2008; Katoh & Omura, 2007, 2013; Lu et al., 2019; Nunn, 1986; Nunn et al., 2009; Omura et al., 2008; Tao et al., 2012, 2017). The nonlinear theory of chorus wave generation has shown that the magnetic field inhomogeneity controls the formation of an electron hole near the velocity of cyclotron resonance (Karpman et al., 1974; Nunn, 1974), producing a resonant current that leads to a concomitant increase of wave amplitude and frequency (e.g., Hikishima & Omura, 2012; Omura et al., 2008, 2013; Shklyar & Matsumoto (2009); Summers et al., 2013). The temporal variation of ~10 – 1000 keV electron precipitation induced by chorus waves was found to depend on the separation between successive rising tone elements (Chen et al., 2020; Miyoshi et al., 2015; Saito et al., 2012).

However, high resolution waveform measurements on board Cluster and Time History of Events and Macroscale Interactions during Substorms (THEMIS) spacecraft, and the Van Allen Probes, have revealed

© 2021. American Geophysical Union. All Rights Reserved.

the presence of a fine structure inside long rising tone chorus waves, consisting of subpackets of various amplitudes and duration (Cattell et al., 2008; Santolík, Kletzing, et al., 2014; Santolík et al., 2003; Wilson et al., 2011). The corresponding wave amplitude modulations were found to significantly affect, and potentially reduce, the nonlinear trapping-induced acceleration of cyclotron resonant relativistic electrons by intense chorus waves in the case of isolated and independent packets/subpackets (Kubota & Omura, 2018; Mourenas et al., 2018; Tao et al., 2013).

Recent statistics of chorus wave packet properties obtained from Van Allen Probes and THEMIS measurements have further shown that short packets represent the overwhelming majority of the observed lower band chorus packets (X. J. Zhang et al., 2018; X. J. Zhang et al., 2019; X. J. Zhang, Mourenas, et al., 2020; Mourenas et al., 2018). In particular, X. J. Zhang, Mourenas, et al. (2020); X. J. Zhang, Agapitov, et al. (2020) found that wave frequency and phase vary very fast and randomly near the edges of most wave packets (or subpackets), especially for short packets of length $\beta < 10 - 30$ (in number of wave periods). Using realistic wave packet properties, X. J. Zhang, Agapitov, et al. (2020) showed that nonlinear electron acceleration is strongly reduced in the presence of such strong wave frequency/phase jumps between successive packets, leading to a more advective or diffusive-like electron energization, as in the case of an interaction with an ensemble of isolated and independent short wave packets (Mourenas et al., 2018).

These recently discovered statistical characteristics of the fine structure of chorus waves should be compared with results from simulations of nonlinear chorus wave generation to check whether these different codes can accurately reproduce all the observed features. This is the main goal of the present work. Verifying the reliability of simulations in reproducing realistic chorus waves is important to assess whether these codes can be safely used to understand and predict the dynamics of electrons interacting with chorus waves in the radiation belts and in the plasma sheet. In particular, it will allow to determine the approximate domains of wave packets parameters covered by each specific code, as compared to the full parameter domain of the observed chorus wave packets.

In the next section, we first provide a brief description of Van Allen Probes and THEMIS chorus wave measurements. We also discuss the different characteristics of the four codes of chorus wave generation examined in this work. These four codes are well-known legacy codes from four different teams, which have been developed and used over many years to study chorus wave generation. The next sections focus on detailed comparisons between the characteristics (peak amplitudes, sizes, frequency sweep rates) of chorus wave packets produced by these four codes and the corresponding statistics of chorus wave packets obtained from multiple years of spacecraft observations near the magnetic equator in the inner magnetosphere.

2. Datasets of Spacecraft Observations and Numerical Models

2.1. Van Allen Probes and THEMIS Measurements

We use the full dataset (2012–2019) of Van Allen Probes (Mauk et al., 2013) waveform measurements of chorus waves at $L \sim 3.5 - 6.5$ (mainly at $L \sim 4.3 - 5.8$) and 5 years of THEMIS spacecraft (Angelopoulos, 2008) waveform measurements in the burst mode at $L \sim 5 - 10$, both obtained near the magnetic equator. We focus on lower-band chorus waves with low wave normal angles (<25°). We use measurements from the Electric and Magnetic Field Instrument Suite and Integrated Science Waves instrument (Kletzing et al., 2013) providing three components of wave electric and magnetic fields on board the Van Allen Probes. Measurements within the plasmasphere are excluded based on the determination of the electron plasma frequency from the upper hybrid resonance frequency line in the 10–400 kHz range (Kurth et al., 2015). Measurements from the THEMIS search coil magnetometer (Le Contel et al., 2008) provide three-component magnetic field fluctuations and waves between 0.1 Hz and 4 kHz and measurements from THEMIS Electric Field Instrument provide three-component waveforms up to 16 kHz (Bonnell et al., 2008), while the fluxgate magnetometer (Auster et al., 2008) data are used to obtain the background magnetic field.

Accurately evaluating the fast nonlinear acceleration of electrons up to MeVs by intense chorus waves is a crucial problem for understanding and modeling the dynamics of the outer radiation belt (Albert, 2002; Demekhov et al., 2009; Kubota & Omura, 2018; Omura et al., 2013; Vainchtein et al., 2018). Since strong variations of wave amplitude, phase, and frequency (possibly also wave normal) can control the efficiency of nonlinear electron acceleration by chorus waves (Kubota & Omura, 2018; Tao et al., 2013; X. J. Zhang,

Agapitov, et al., 2020), it is more appropriate to directly examine the time series of the wave magnetic amplitude (the waveform), rather than inspecting separate long rising tone chorus elements. One should also focus on intense wave packets that may be above the threshold for nonlinear trapping slightly away from the equator (Artemyev et al., 2014; Nunn, 1974; X. J. Zhang et al., 2019).

In the present study, we therefore select wave packets with peak full amplitudes $B_{w,peak} > 50$ pT, with wave packet size β calculated as the number of wave periods between the nearest dips in full wave amplitude below a fixed threshold of 50 pT (or at 10 pT if the amplitude dip is lower) on each side of the peak, as in previous works (X. J. Zhang, Agapitov, et al., 2020; X. J. Zhang, Mourenas, et al., 2020). Note that wave packets defined this way can correspond either to isolated wave packets, or to subpackets inside a traditional long rising tone chorus element, or, more rarely, to long rising tone chorus packets which contain only moderate internal amplitude modulations. Using an alternative definition of wave packet length at half of their peak amplitude as in our previous work (X. J. Zhang et al., 2019) would have led to a larger fraction of short packets, but with the important inconvenience that many packets would be artificially truncated at an amplitude much higher than the peak amplitude of other packets (note that using a threshold defined as a small fraction of $B_{w,peak}$ is often impossible due to the high level of non-coherent wave noise around intense wave packets). We settled for a 50 pT threshold because this is also close to the minimum wave amplitude needed to reach the regime of nonlinear wave-particle interaction (Artemyev et al., 2014; X. J. Zhang et al., 2019). Using a lower threshold would often result in the classification of a long train of well separated wave packets as a single long packet, missing the fine structure of chorus waves that we wish to examine. Alternatively, using a higher threshold (e.g., 200 pT, see X. J. Zhang et al., 2018) would exclude many moderate amplitude packets. Figures 1a, 1b, 2a, and 2b provide typical examples of long and short lower band chorus wave packets measured by the Van Allen Probes and THEMIS spacecraft, respectively at $L = 5.8$ in the heart of the outer radiation belt and at larger distances from the Earth ($L \simeq 7.1$).

2.2. Backward-Wave-Oscillator Model

The backward-wave-oscillator (BWO) model (Demekhov, 2011; Demekhov & Trakhtengerts, 2008; Demekhov et al., 2017) assumes a transition from convective to absolute cyclotron instability in the presence of a step-like deformation in the parallel (to the geomagnetic field) velocity distribution of energetic electrons (this deformation may naturally occur in the presence of cyclotron generation of very low amplitude waves). This absolute instability is similar to a backward-wave-oscillator, due to the opposite direction of wave group velocity and resonant electron velocity. The waves propagate along a realistic geomagnetic field line with parabolic inhomogeneity. There is a set of approximations: (a) The BWO is assumed to have a low efficiency, for which variations of parallel electron velocity with respect to their initial values are taken into account only as an effect of electron escaping from the resonance, (b) the electron velocity distribution is assumed to possess a narrow maximum at a given transverse energy, and (c) the cold plasma density is assumed to vary like the background magnetic field strength. These approximations allow to derive a simplified system of equations (Demekhov & Trakhtengerts, 2008). In the present simulation, we consider $L \sim 7$, a cold plasma density $n_c = 5\ \mathrm{cm}^{-3}$, a wave frequency to gyrofrequency ratio of $f/f_{ce} \sim 0.25$, $f_{ce} \approx 2.86$ kHz, and a transverse velocity $V_\perp$ of electrons equal to their cyclotron resonant parallel velocity. The initial wave amplitude is 0.15 pT for a wave refractive index of 18.3 (plasma frequency to gyrofrequency ratio $f_{pe}/f_{ce} \sim 8$). Other parameters are described in detail in Demekhov et al. (2017). After their nonlinear growth, the simulated rising tone chorus waves reach peak amplitudes of 800–1,000 pT at the boundary of generation region, ≈3600 km away from the equator. For our analysis we use wave fields collected at this location and right at the equator. Figures 1c and 2c show typical examples of long and short wave packets from this simulation, generated in the equatorial source region (less than 4,000 km from the equator).

2.3. DAWN Hybrid Model

The DAWN hybrid code models cold electrons through linearized fluid equations and energetic electrons by particle-in-cell techniques (Tao, 2014) or nonlinear delta-f methods (Tao et al., 2017). The energetic electron distribution is modeled by a bi-Maxwellian with density n_h. The background magnetic field is

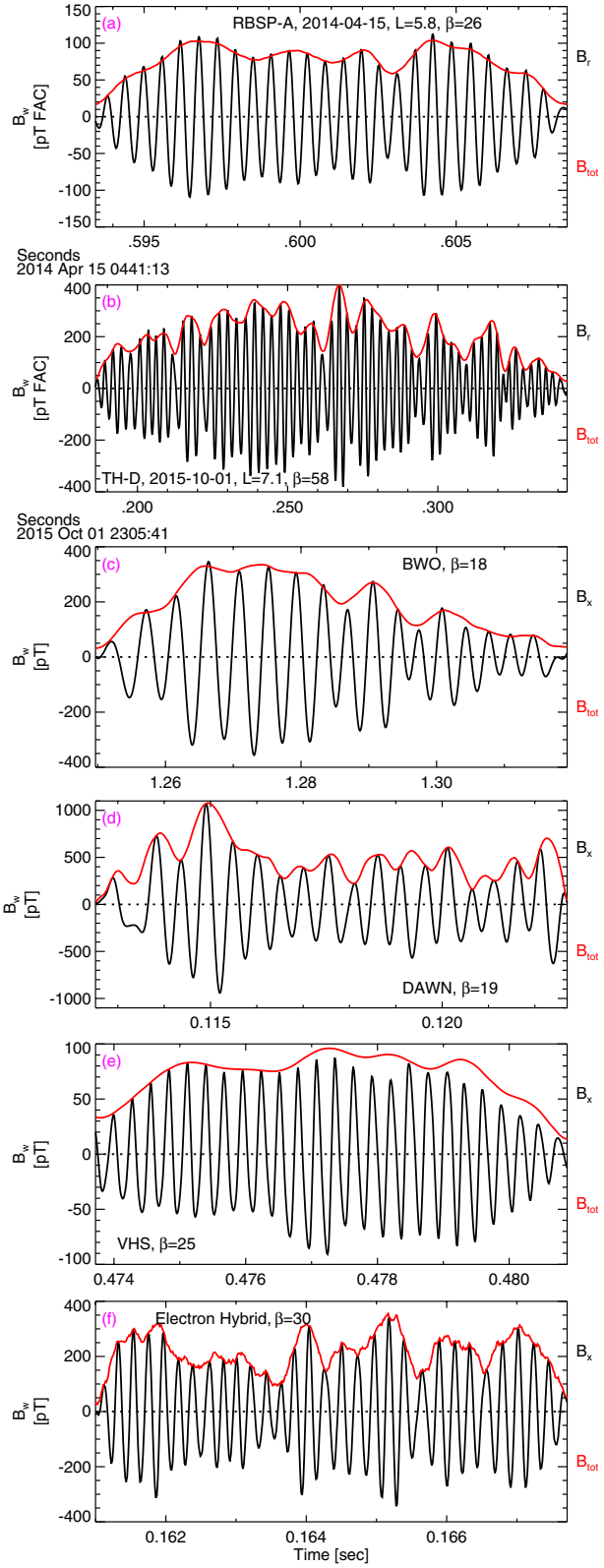

Figure 1. Various examples of long chorus wave packets (a and b) wave packets measured by the Van Allen Probes and Time History of Events and Macroscale Interactions during Substorms spacecraft, respectively; (c) wave packet produced by the backward-wave-oscillator code; (d) wave packet produced by the DAWN hybrid code; (e) wave packet produced by the Vlasov hybrid code; (f) wave packet produced by the electron hybrid code.

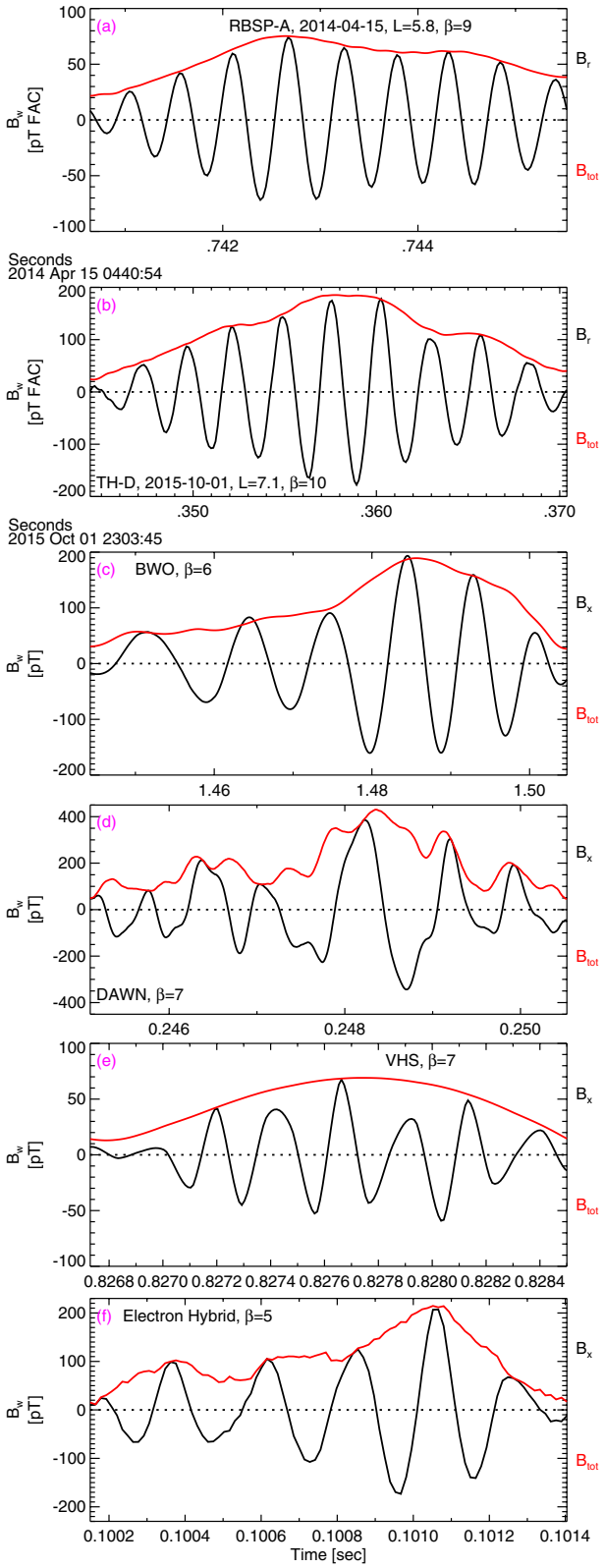

Figure 2. Various examples of short chorus wave packets (a and b) wave packets measured by the Van Allen Probes and Time History of Events and Macroscale Interactions during Substorms spacecraft, respectively; (c) wave packet produced by the backward-wave-oscillator code; (d) wave packet produced by the DAWN hybrid code; (e) wave packet produced by the Vlasov hybrid code; (f) wave packet produced by the electron hybrid code.

assumed to be nearly dipolar and the generated chorus waves are parallel propagating from the magnetic equator. Full details on the DAWN code are provided in Tao (2014); Tao et al. (2017); Tao et al. (2020); Wu et al. (2020).

In the present simulation, we use the same parameters as in previous studies (Tao, 2014; Tao et al., 2017). To speed up computer calculations, we use a reduced scale length of the geomagnetic field inhomogeneity (equivalent to a reduced planet size) such that $B(z) = B_0(z = 0)(1 + \xi z^2)$, with $\xi = 4.5/(LR_p)^2$, with z the distance to the equator, $R_p = R_{Earth}/32$ the planet size, and $L = 4$ (and corresponding $f_{ce} \approx 14$ kHz). The time step is $0.02/\Omega_{ce}$ and there are 5×10^5 time steps, 6,554 cells of size $0.05c/\omega_{ce}$, 2,000 electrons per cell, with $f_{pe}/f_{ce} = 5$, $n_h/n_c = 0.006$, parallel thermal velocity $v_{\parallel} = 0.2c$, and transverse thermal velocity $v_{\perp} = 0.53c$. The simulation leads to the nonlinear generation of rising tone chorus waves at $f/f_{ce} \simeq 0.25 - 0.5$ reaching peak amplitudes of 800 pT at ≈800 km away from the equator. For our analysis we use wave fields collected at five locations: ∼114 km, ∼228 km, ∼456 km, ∼912 km, and ∼1368 km away from the equator. Note that the background magnetic field gradient, and its rescaling, may influence the wave growth rate and the full length of a chorus element (e.g., see Demekhov & Trakhtengerts, 2008; Tao et al., 2014), but should not significantly affect much smaller scales (i.e., scales of individual wave packets) which are determined by modulations of the wave envelope. Figures 1d and 2d show typical examples of long and short wave packets from this simulation, generated in the equatorial source region (around 228 km away from the equator). In Figure 2d, irregular oscillations of the wave amplitude probably indicate a superposition of several waves of different amplitudes that, together, form a short wave packet (Nunn et al., 2021; Tao et al., 2013; X. J. Zhang, Mourenas, et al., 2020). In the present study, all wave packets are kept in both spacecraft and model datasets, without singling out quasi-monochromatic waves, because our main goal here is to compare the fine packet/subpacket structure of chorus waves in observations and simulations.

2.4. Vlasov Hybrid Model

The Vlasov hybrid simulation (VHS) code is one-dimensional along the realistic inhomogeneous (parabolic) geomagnetic field, assuming parallel propagating waves starting to grow from the equatorial zone (Nunn et al., 2005, 2009). The simulation box goes from $z = -10000$ km to $z = +10000$ km. In the present simulation, we consider $L \sim 4$ outside the plasmasphere with $n_c = 5.4$ cm^{-3}, $f_{ce} = 15$ kHz, $f_{pe}/f_{ce} \simeq 1.5$, with a keydown triggering wave of 10 pT at base frequency of 6.375 kHz introduced at $z = -10000$ km. The anisotropic hot electron distribution consists of two bi-Maxwellians: the first one with $n_h = 3 \times 10^{-4} n_c$, $T_{\perp} = 34$ keV, $T_{\parallel} = 15$ keV, and the second one with $n_h = 9 \times 10^{-3} n_c$, $T_{\perp} = 192$ keV, $T_{\parallel} = 60$ keV. This distribution function is scaled to give the desired value of linear growth rate of 280 dB/s at the equator at the triggering (base) frequency. The VHS code neglects the dispersion effect with constant wave phase velocity and group velocity, and advances the wavefield with the narrow band wavefield equation at the base frequency. The nonlinearly generated rising tone chorus waves reach peak amplitudes of 150 pT at the boundary of the generation region, ≈6000 km away from the equator. For our analysis we use wave fields collected at this location. Figures 1e and 2e show typical examples of long and short wave packets from this simulation, generated in the equatorial source region (between –2000 km and +6000 km around the equator).

2.5. Electron Hybrid Model

The electron hybrid code treats cold electrons as a fluid and energetic electrons as particles treated via the standard particle-in-cell method with relativistic effects (Katoh & Omura, 2004, 2013, 2016). This code has reproduced the generation process of chorus with rising tones (Katoh & Omura, 2016; Omura et al., 2008). The system is one-dimensional along a realistic dipolar geomagnetic field line such that $B(z) = B_0(1 + \xi z^2)$, with $\xi = 4.5/(LR_{Earth})^2$ at $L = 4$ (and corresponding $f_{ce} \approx 14$ kHz). The parameters of the simulation are the same as in Katoh and Omura (2016). The number of grid points is 65,536 and the spatial extent of the simulation is 18,500 km from the magnetic equator in both hemispheres. The plasma frequency to gyrofrequency ratio is $f_{pe}/f_{ce} = 2.4$. The 1 billion energetic electrons have an anisotropic initial velocity distribution with a density equal to $n_h = 9.9 \times 10^{-4} n_c$, leading to whistler-mode wave generation at frequen-

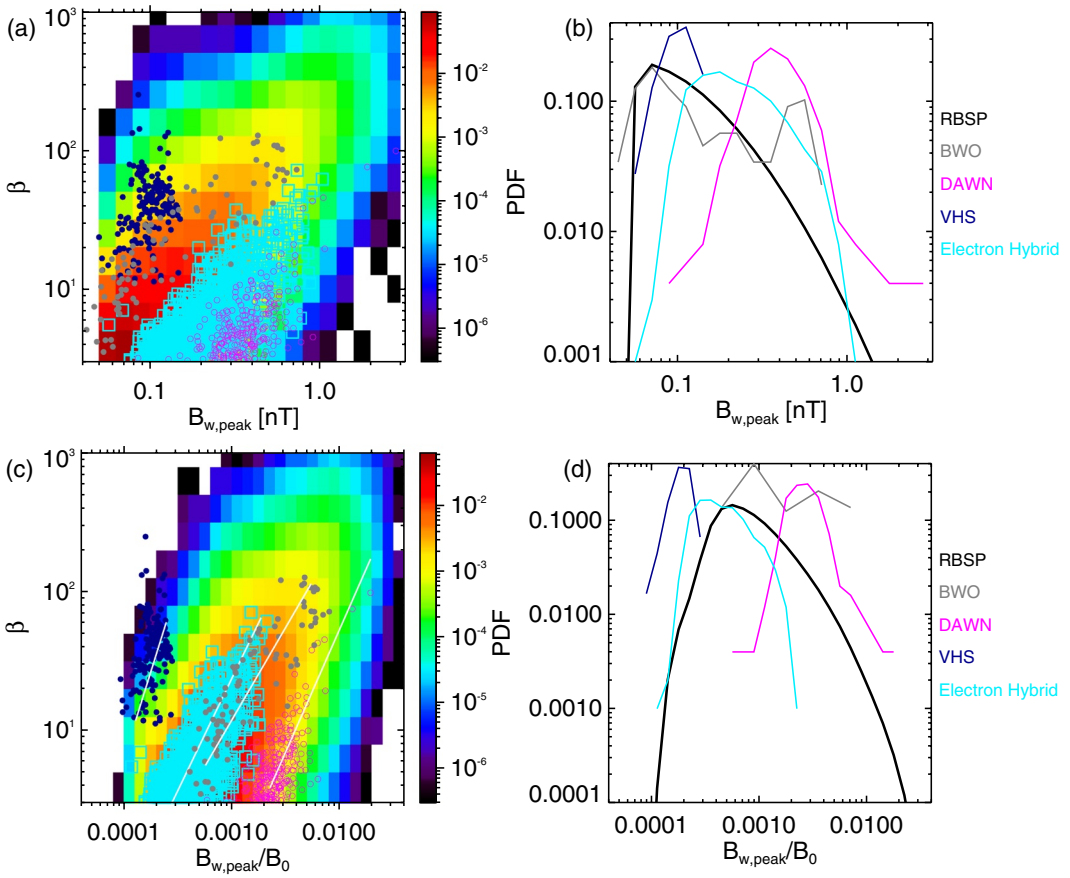

Figure 3. (a) Distributions in the $(B_{w,peak}, \beta)$ space of wave packets from the backward-wave-oscillator code (gray circles), from the DAWN code (purple empty circles), from the Vlasov hybrid simulation code (dark blue circles), and from the electron hybrid code (light blue squares). Statistical results from 2012 to 2019 Van Allen Probes observations show the probability of wave packets to be inside a given $(B_{w,peak}, \beta)$ bin (color scale). (b) Probability distribution function of wave packets as a function of $B_{w,peak}$, for the Van Allen Probes (thick black curve) and the four different codes (same colors as in panel (a)). (c) Same as (a) in the $(B_{w,peak}/B_0, \beta)$ space, with B_0 the equatorial background magnetic field strength. White lines show fits of the form $\beta \sim (B_{w,peak}/B_0)^A$ for each code, with corresponding exponents A given in the text (only packets with $|\partial f/\partial t| < f^2/2$ are shown). (d) Same as (b) but as a function of $B_{w,peak}/B_0$.

cies $f/f_{ce} = 0.25 - 0.5$. There is both a loss cone anisotropy and a temperature anisotropy, with parallel and transverse thermal momenta $U_{th\|} = 0.2705c$ and $U_{th\perp} = 0.46852c$, respectively. Figures 1f and 2f show typical examples of long and short wave packets from this simulation, generated in the equatorial source region (within 800 km of the equator). For our analysis we use wave fields collected at the equator and at 800 – 1600 km away from the equator.

3. Wave Packet Sizes and Peak Amplitudes

3.1. Full Distributions

The distributions in $(B_{w,peak}, \beta)$ space of chorus wave packets from the backward-wave-oscillator code, the DAWN code, the VHS code, and the electron hybrid code are shown in Figure 3. Wave packets obtained within ~1000 – 6000 km from the magnetic equator are shown. In addition, statistics from Van Allen Probes observations at $L \sim 4.3 - 5.8$ in 2012–2019 show the full distribution of observed lower-band chorus wave packets collected within ~6° of the geomagnetic equator, that is, less than 3,500 km from the equator. Sta-

tistics from THEMIS measurements, which cover higher L-shells ($5 < L < 10$), are very similar to Van Allen Probes results (X. J. Zhang, Mourenas, et al., 2020).

Figures 3a and 3b show that wave packets from the four different codes recover well the $(B_{w,peak},\beta)$ domain (in yellow to red) corresponding to the main population of observed chorus wave packets, although each simulation recovers different portions of this full $(B_{w,peak},\beta)$ domain. The VHS, BWO, electron hybrid, and DAWN simulations, in this order, cover progressively larger amplitudes $B_{w,peak}$ for constant β in Figures 3a and 3b and tend also toward smaller β values. The probability distribution functions (PDF) of $B_{w,peak}$ of wave packets from the VHS simulation is similar to the statistical distribution from Van Allen Probes observations in Figure 3b, with a peak at ∼65 – 150 pT, while wave packets from the electron hybrid simulation have slightly higher amplitudes $B_{w,peak} \sim 80 - 500$ pT than in observations. The PDF of $B_{w,peak}$ from the BWO simulation has two peaks, one recovering the PDF of observations, but also another one of nearly the same magnitude at larger $B_{w,peak} \sim 500$ pT, corresponding to much more frequent intense packets in the simulation than in statistical observations. Finally, the PDF of $B_{w,peak}$ from the DAWN simulation has one broad peak at peak amplitudes ∼150 – 650 pT higher than in statistical observations. Van Allen Probes statistics show that most observed wave packets have $B_{w,peak} \sim 60 - 250$ pT, with much more rare wave packets up to 1–2 nT.

The different peak amplitudes of wave packets in the different simulations and in observations in Figure 3b are likely mainly related to the different parameters of cold plasma and geomagnetic field (L-shell or f_{ce}, f_{pe}/f_{ce}, ξ) and of the anisotropic energetic electron distributions used in the different simulations (to keep typical parameters previously explored with each code), because such parameters correspond to different wave growth rates and final amplitudes. In this regard, it is worth emphasizing that initial parameters for each simulation cover only a small portion the full range of cold plasma and electron distribution parameters corresponding to actual observations. Besides, using different amplitudes for the initial triggering waves in the simulations is known to have a very weak impact on the final characteristics of the triggered waves (Hikishima & Omura, 2012). Figures 3c and 3d show the same results as a function of wave packet peak amplitude $B_{w,peak}/B_0$ normalized to the equatorial background magnetic field strength B_0 to take into account the different L-shells covered in simulations and observations. With this normalization, wave packets from the electron hybrid simulation (performed at $L = 4$ vs. $L \sim 4.5 - 5.8$ in observations) recover well the main population of observed chorus wave packets. However, the distributions of wave packets from the other simulations are only slightly shifted compared with observations. Thus, wave packet amplitudes are mostly determined by parameters of the anisotropic energetic electron distribution in the wave source region (or by the corresponding wave growth rate), and depend less on the background magnetic field characteristics.

When considering the position of wave packets in the $(B_{w,peak},\beta)$ space in Figures 3a and 3c, the backward-wave-oscillator code recovers well the main region of observed chorus wave packets. In particular, it recovers well the domain of the observed intense wave packets, which are more rare (∼5% of all the packets) but generally longer ($\beta \sim 40 - 100$) than less intense packets, because this code was mainly designed to model such intense chorus wave packets. Wave packets from the VHS simulation reach slightly smaller sizes ($\beta \sim 10 - 75$) and are less intense. The DAWN and electron hybrid simulations mostly cover the range $\beta \sim 3 - 20$ of the main population of chorus wave packets observed by satellites (representing ∼95% of all packets), but with slightly higher average amplitudes ($B_{w,peak} \sim 0.1 - 0.6$ nT). With its higher ξ value used in this simulation than in reality, the DAWN code was expected to produce more intense waves than in observations (Katoh & Omura, 2013; Tao, 2014).

Notwithstanding these differences, it is worth emphasizing that all four simulations successfully reproduce the general physical trend of packet size β increase like $\beta \sim B_{w,peak}^{3/2}$ as in statistics of chorus wave packets from the Van Allen Probes observations (see Figures 3a and 3c). The slopes obtained from least squares linear fitting of the data shown in Figure 3c are: $\beta \sim B_{w,peak}^{1.7\pm1.2}$ (DAWN), $\beta \sim B_{w,peak}^{2.5\pm1.5}$ (VHS), $\beta \sim B_{w,peak}^{1.6\pm1.2}$ (electron hybrid code), $\beta \sim B_{w,peak}^{1.3\pm1.0}$ (BWO) (these slopes are obtained by fitting median $B_{w,peak}/B_0$ values in each β bin). The wave packet size β, calculated as the number of wave periods during which the full wave amplitude remains above a fixed threshold of 50 pT, becomes larger due to the higher peak amplitude. The observed trend is consistent with an average wave packet shape $B_w(t)/B_{w,peak} \approx \epsilon/(|t - t_{peak}|^{2/3} + \epsilon)$ down to $B_w = 50$ pT (the threshold for determining packet size), with $\epsilon \ll \max(|t - t_{peak}|^{2/3})$ and t_{peak} the time

when the packet reaches its peak amplitude. This corresponds to wave packets with an amplitude decreasing more and more slowly away from the peak, like for many wave packets from both observations and simulations shown in Figures 1 and 2.

Figure 4 shows the variation of the distributions of wave packets in the $(B_{w,peak},\beta)$ space, as a function of the distance from the magnetic equator, in observations and for the four different simulations. Note that in all simulations, the maximum distance from the equator is ∼1000 − 6000 km, implying that all wave packets probably remain within the region of sustained nonlinear chorus wave growth (Demekhov & Trakhtengerts, 2008; Omura et al., 2008).

In all simulations, both the size β and peak amplitudes $B_{w,peak}$ of wave packets are found to increase on average from the equator to a distance of ≈1000 − 6000 km from the equator. This is especially well seen in the electron hybrid simulation in Figures 4g and 4h and in the DAWN simulation in Figures 4c and 4d. It is likely due to the nonlinear convective growth of the wave amplitude as the waves propagate away from the equator (Omura et al., 2008). The wave packet size, calculated above a fixed threshold of 50 pT, becomes larger due to the higher peak amplitude (for roughly similar average packet shapes). The frequency sweep rate $\partial f/\partial t$ of wave packets seems to decrease in general as β increases for a given amplitude range.

3.2. Rising and Falling Frequency Wave Packets

Figure 5 shows the distributions in the $(B_{w,peak},\beta)$ space of chorus wave packets, separately for packets with rising frequency ($\partial f/\partial t > 0$) and falling frequency ($\partial f/\partial t < 0$), for the four simulations and satellite observations. Inside each wave packet from observations and simulations selected with $B_{w,peak} > 50$ pT, the frequency sweep rate $\partial f/\partial t$ was determined through linear regression, using wave half-periods calculated between two successive zeros of one transverse component of the wavefield (X. J. Zhang, Mourenas, et al., 2020). Note that falling and rising frequency wave packets are classified here by the frequency variation within each wave packet, and that these wave packets are often much shorter than a full chorus element – which generally lasts more than 0.1 s and includes many of such wave packets (or subpackets). Therefore, the presence (or absence) of falling and rising frequency wave packets is not necessarily related to the presence (or absence) of full falling and rising tone chorus elements in spacecraft and model datasets.

For the traditional long ($\beta > 30 - 50$, or $> 0.05 - 0.1$ s) rising or falling tones discussed in many past studies (Burtis & Helliwell, 1976; Li, Thorne, et al., 2011), satellite statistics have demonstrated that such long rising tones are ∼10 − 20 times more frequent than long falling tones and have quasi-parallel wave normal angles, contrasting with the more oblique wave normal angles (>60°) of long falling tones in general (Li, Thorne, et al., 2011; Taubenschuss et al., 2014). Both Van Allen Probes observations in 2012–2019 and simulations in Figure 5 confirm that the longest (and more rare) quasi-parallel wave packets with $\beta > 30 - 40$ more frequently correspond to rising tones than falling tones. Based on previous simulations and theoretical works in a realistic dipolar magnetic field configuration (Nunn & Omura, 2012), quasi-parallel long falling tones should correspond to the formation of an electron hill in which more electrons are trapped in the wave potential, upstream from the equator. Effective entrapping then takes place at the wavefront, which should correspond to not-too-long wave packets for such falling tones. For very long wave packets, an electron hole should usually develop instead, corresponding to long rising tones (Hikishima & Omura, 2012; Omura et al., 2008). Both observation and some simulations in Figure 5 seem to roughly confirm this general trend for the longest wave packets with $\beta > 30 - 40$. The obliquity of such long falling tones cannot be reproduced by the present one-dimensional codes, but ray-tracing simulations have shown that parallel long falling tones generated upstream from the equator (Nunn & Omura, 2012) should become significantly oblique after crossing the equator, as in observations (Yamaguchi et al., 2013).

But let us now examine the much more frequent rising or falling frequency *short wave packets*, which have much shorter sizes ($\beta < 30$, or $< 0.03 - 0.05$ s) than the long rising and falling tones considered in many past studies. In the case of such intense short wave packets with quasi-parallel wave normal angles, Van Allen Probes observations have shown the presence of similar quantities of packets with rising and falling frequency (X. J. Zhang, Mourenas, et al., 2020). The four simulations in Figure 5 also show the presence of similar amounts of rising and falling frequency short packets, in agreement with statistical observations.

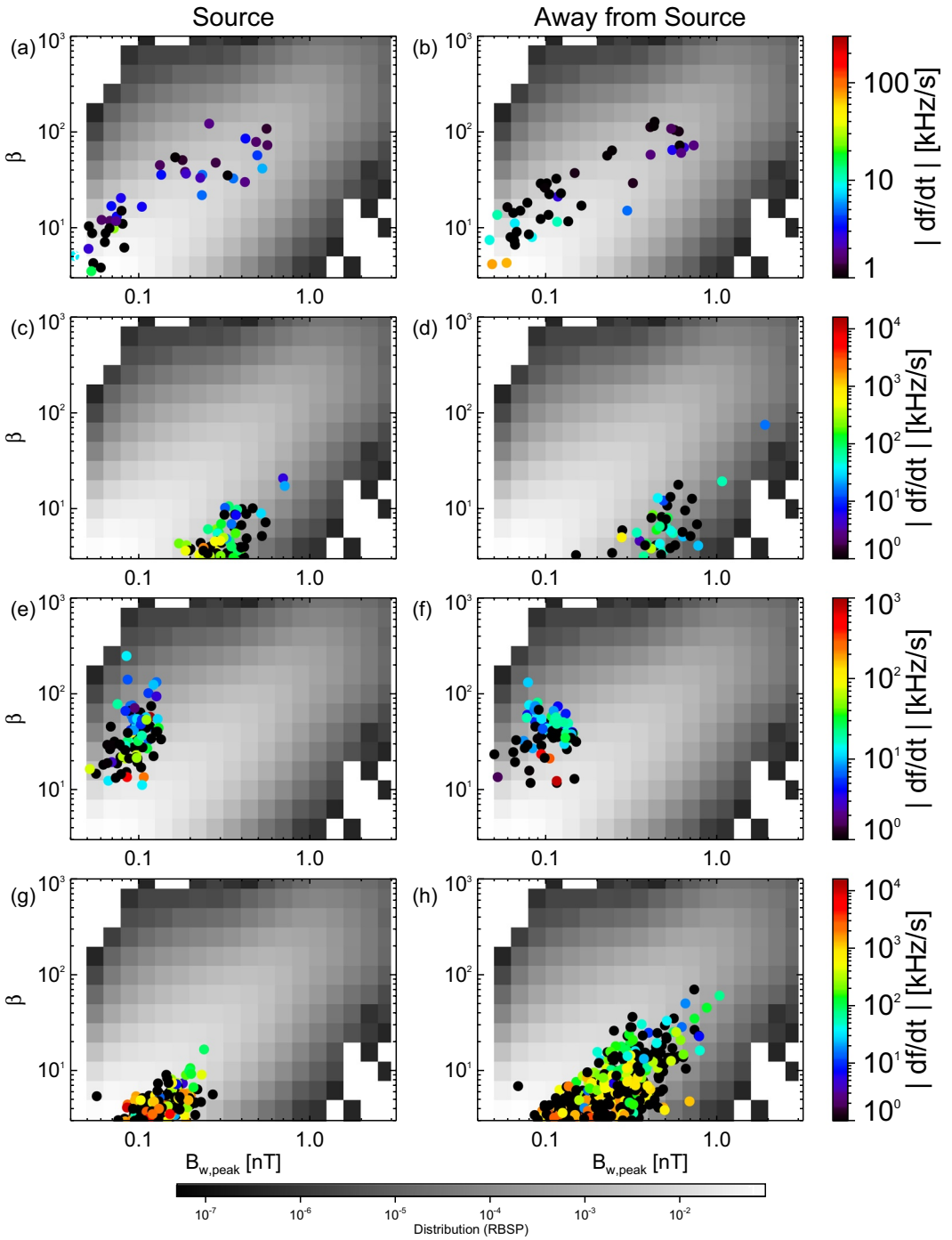

Figure 4. (a) Distributions in the $(B_{w,peak}, \beta)$ space of wave packets from the backward-wave-oscillator code in the equatorial source region. Statistical results from 2012 to 2019 Van Allen Probes observations show the probability of wave packets to be inside a given $(B_{w,peak}, \beta)$ bin (gray scale). Colors give the sweep rate $\partial f/\partial t$ of wave packets from the simulation (only packets with $|\partial f/\partial t| < f^2/2$ are shown). (b) Same as (a) but ~3600 km away from the magnetic equator. (c and d) Same as (a and b) for wave packets from the DAWN code (at 245 and 1,000 km from the equator, respectively). (e and f) Same as (a and b) for wave packets from the VHS code (near equator and at 6,000 km from the equator, respectively). (g and h) Same as (a and b) for wave packets from the electron hybrid code (at 0 and 1,100 km from the equator, respectively).

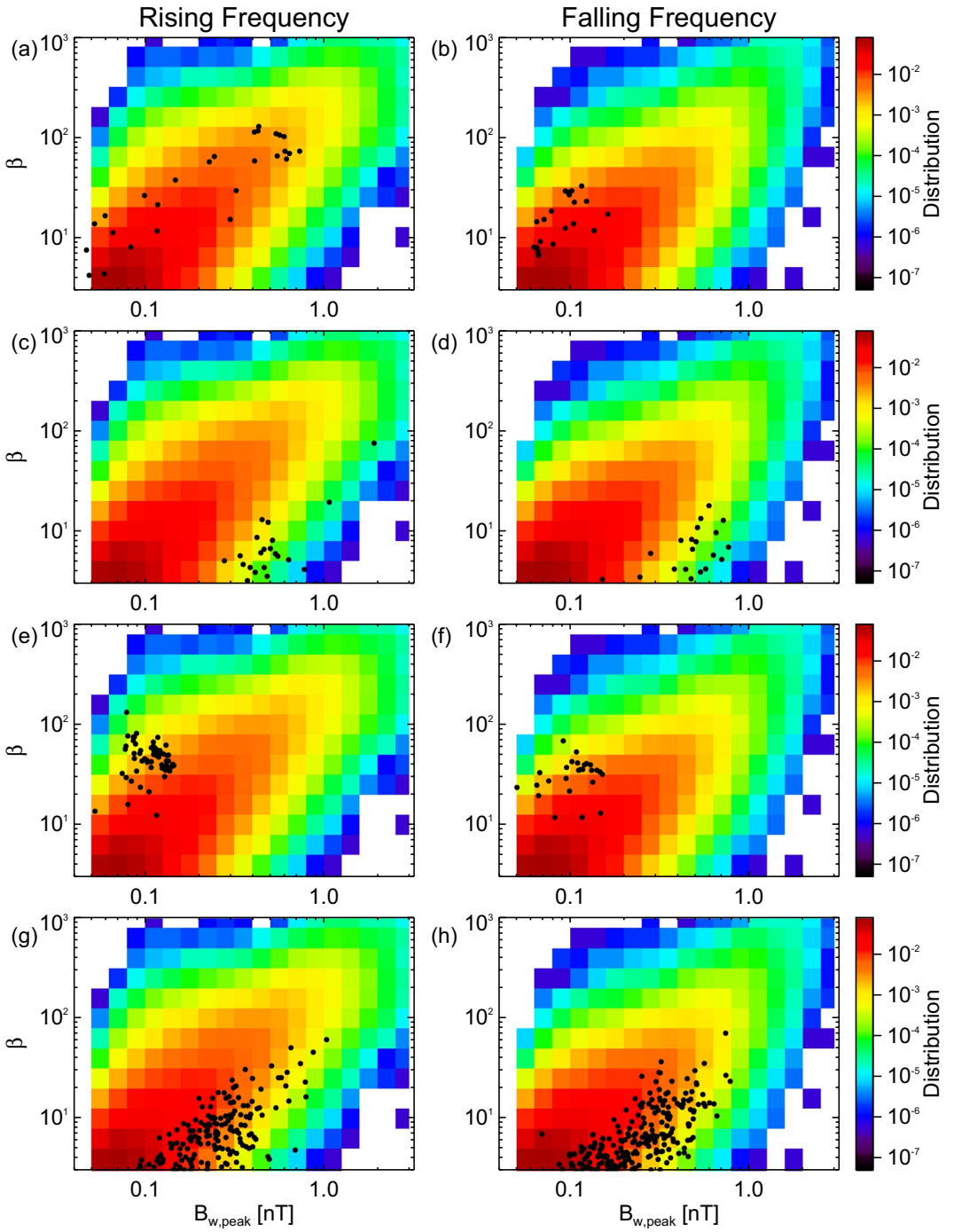

Figure 5. (a) Distributions in the $(B_{w,peak}, \beta)$ space of rising frequency wave packets from the backward-wave-oscillator code at some distance (~1000 – 3600 km) from the magnetic equator (black circles). Statistical results from 2012 to 2019 Van Allen Probes observations show the probability of rising frequency wave packets to be inside a given $(B_{w,peak}, \beta)$ bin (color scale). (b) Same as (a) but for falling frequency packets. (c and d) Same as (a and b) for wave packets from the DAWN code. (e and f) Same as (a and b) for wave packets from the Vlasov hybrid simulation code. (g and h) Same as (a and b) wave packets from the electron hybrid code.

Such rising and falling frequency short packets could be formed through nonlinear amplitude modulation at the trapping frequency, potentially leading to a faster frequency variations at packet edges inside the shortest packets (Morales & O'Neil, 1972; Tao et al., 2017). Alternatively, they could result from wave superposition whenever two or more waves are simultaneously present with similar amplitudes and a sufficiently large frequency difference, leading to fast frequency variations near packet edges (Tao et al., 2013; X. J. Zhang, Agapitov, et al., 2020; X. J. Zhang, Mourenas, et al., 2020). These two different mechanisms might explain the very large sweep rates $\partial f/\partial t > 40$ kHz/s often obtained for $\beta < 20$ in both observations and simulations in Figure 5. The next section will be devoted to a closer examination of frequency sweep rates.

4. Wave Packet Sizes and Frequency Sweep Rates

Let us first remind the reader that Van Allen Probes chorus wave data is taken at low latitudes (<6°) within the generation region close to the equator, and that we mainly examine relatively short packets ($\beta < 25-50$) instead of the traditional long rising tone chorus elements studied in many past works. For long rising tones, frequency sweep rate theory is already well advanced (Demekhov & Trakhtengerts, 2008; Nunn, 1974; Omura et al., 2008; Vomvoridis et al., 1982; Wu et al., 2020) and tested (Cully et al., 2011; Macúšová et al., 2010; Nunn et al., 2009; Tao et al., 2012). However, the physical processes governing frequency sweep rates inside relatively short wave packets (or subpackets) may be different from the processes controlling average frequency sweep rates of long rising tone chorus elements ($\beta > 100-150$). Long rising tones have generally moderate and mostly positive $\partial f/\partial t$ values calculated by linear regression over their full duration (X. J. Zhang, Mourenas, et al., 2020), partly due to a smoothing of frequency variation over a very long time period. In contrast, the wave frequency varies more strongly and more randomly inside short packets, with nearly as many rising and falling frequency packets (X. J. Zhang, Mourenas, et al., 2020). In this case, $\partial f/\partial t$ can be much larger than the typical frequency variation of an individual wave, because f is determined as half the inverse of the time interval between two successive zero crossings of one transverse magnetic amplitude component in the full time series, and this magnetic component may then result from a superposition of different waves of varying amplitudes (X. J. Zhang, Mourenas, et al., 2020).

Figure 6a shows the distribution of wave packets in the $(\beta, \partial f/\partial t)$ space obtained from the four different codes and from satellite observations. The $(\beta, \partial f/\partial t)$ domains covered by wave packets from the DAWN, electron hybrid, VHS, and BWO simulations are remarkably complementary and, together, they cover nearly the whole parameter region (in yellow to red) containing the majority of the observed chorus wave packets. Wave packets from the simulations do not appear in significant numbers outside this region. The backward-wave-oscillator code recovers well the main region of the observed intense wave packets, located at $\beta = 10-100$ and $\partial f/\partial t \sim 1-10$ kHz/s (in red). The DAWN and electron hybrid simulations cover a different $(\beta, \partial f/\partial t)$ portion of the main domain of statistical observations, at smaller $\beta = 3-15$ and very high sweep rates of $\partial f/\partial t \sim 30-1000$ kHz/s and $\partial f/\partial t \sim 100-3000$ kHz/s, respectively. The VHS simulation reproduces observed wave packets at $\beta \simeq 7-60$ and moderate $\partial f/\partial t \sim 5-500$ kHz/s.

The decrease of the mean sweep rate approximately like $\partial f/\partial t \sim 1/\beta^2$ as β increases in observations is well reproduced by the four simulations. This trend may have two different physical origins. The high amplitude of chorus waves may lead to their amplitude modulation at the trapping frequency (related to momentum and energy conservation in the wave frame; e.g., see Morales & O'Neil, 1972), potentially allowing the formation of packets of finite size $\beta \sim \beta_{tr} = f/f_{tr} \sim 5-20$ (with f_{tr} the trapping frequency) for a typical transverse energy of resonant energetic electrons smaller than 100–150 keV (Tao et al., 2017). This nonlinear mechanism likely explains the generation of some of the short and intense wave packets produced in the different simulations. In particular, the DAWN and electron hybrid simulations produce many short packets with $\beta \simeq 5-20$ and $B_{w,peak} \simeq 0.2-0.5$ nT that correspond to large frequency sweep rates >20 kHz/s. For such intense wave packets, the obtained $\partial f/\partial t$ values roughly correspond to the analytical nonlinear sweep rates $|\partial f/\partial t|_{NL} \simeq |S| f_{tr}^2 = |S| f^2/\beta_{tr}^2$ of chorus waves derived by Vomvoridis et al. (1982), Omura et al. (2008), and Demekhov and Trakhtengerts (2008), where $|S| \sim 0.4$ is the inhomogeneity factor. However, the validity of such analytical expressions of $(\partial f/\partial t)_{NL}$, initially derived under the assumption of a slowly varying wave amplitude (Demekhov & Trakhtengerts, 2008; Omura et al., 2008), may become questionable

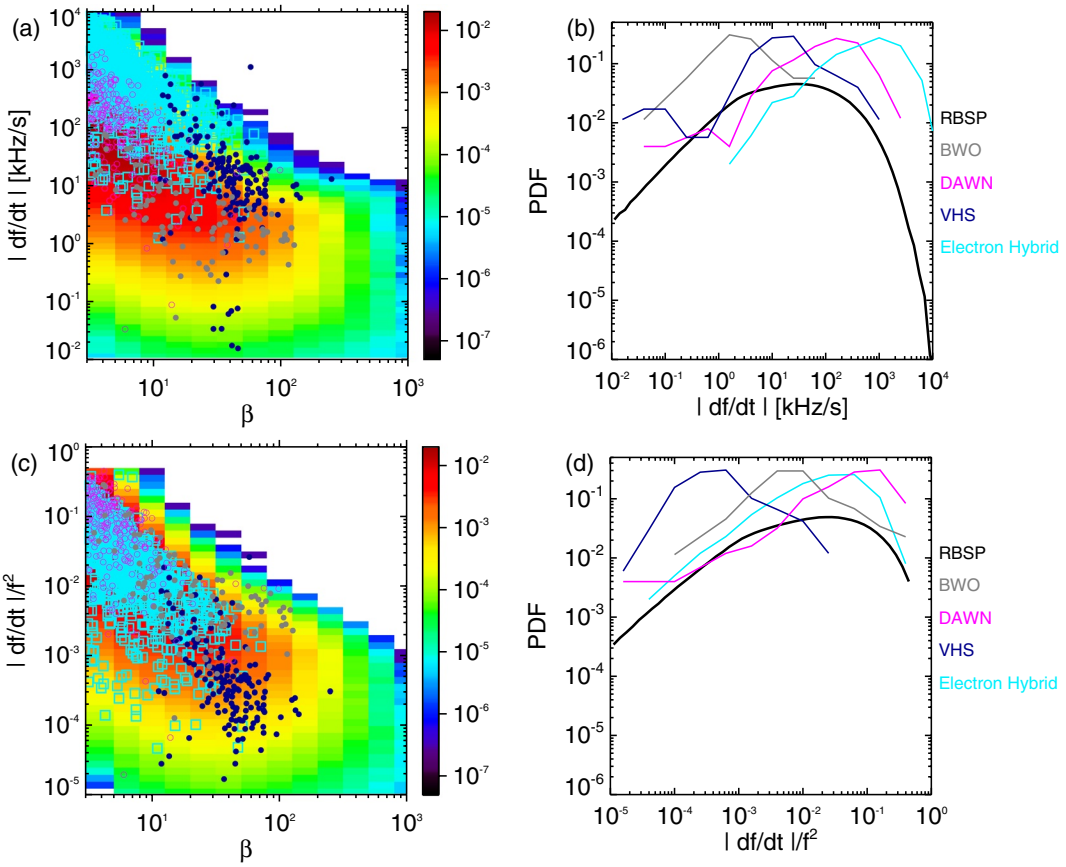

Figure 6. (a) Distributions in the $(\beta, \partial f/\partial t)$ space of wave packets from the backward-wave-oscillator code (gray circles), from the DAWN code (purple empty circles), from the Vlasov hybrid simulation code (dark blue circles), and from the electron hybrid code (light blue squares). Statistical results from 2012 to 2019 Van Allen Probes observations show the probability of wave packets to be inside a given $(\beta, \partial f/\partial t)$ bin (color scale). Only packets with $|\partial f/\partial t| < f^2/2$ are shown. (b) Probability distribution function of wave packets as a function of $\partial f/\partial t$, for the Van Allen Probes (thick black curve) and the four different codes (same colors as in panel (a)). (c and d) Same as (a and b) but using the normalized sweep rate $(\partial f/\partial t)/f^2$ in both observations and simulations.

for the shortest packets with $\beta < 5$ obtained in the DAWN and electron hybrid simulations, as well as in satellite observations.

Moreover, the very short wave packets with $\beta \simeq 3-10$ and moderate $B_{w,peak} < 0.3$ nT obtained in the electron hybrid simulation may not result only from an amplitude modulation at the trapping frequency, because for the low $L = 4$ and small $f_{pe}/f_{ce} = 2.4$ used in this simulation, the trapping period should then remain relatively long ($>13/f$), corresponding to amplitude modulations of length $\beta_{tr} > 13$.

How to explain the formation of such very short packets with $\beta < 6$ and low amplitudes $B_{w,peak} < 0.3$ nT? In fact, the spectrum of the electron hybrid simulation (provided in Figure 2b from Katoh & Omura, 2016) shows the presence of not only one, but two simultaneous rising tone chorus waves of similar amplitudes. These two rising tones have a frequency difference $\Delta\omega \approx \omega/5$ that may lead to wave amplitude modulation by wave superposition, forming packets of size $\beta \simeq \omega/\Delta\omega \sim 5$ even for low amplitudes waves (Tao et al., 2013; X. J. Zhang, Mourenas, et al., 2020). Some wave superposition can also be seen at different times in the spectrum from the DAWN code (Tao, 2014; Tao et al., 2017). Wave superposition is often accompanied by sudden and large jumps in packet frequency/phase near packet edges and can lead to a frequency sweep rate inside short packets $|\partial f/\partial t| \sim f^2/\beta^2$ (Nunn et al., 2021; X. J. Zhang, Agapitov, et al., 2020; X. J. Zhang, Mourenas, et al., 2020). Similarly fast positive and negative wave frequency variations at the edges of short chorus wave packets have been found in self-consistent electromagnetic full-particle simulations,

often at times when the spectrum showed the coexistence of waves of moderate amplitudes (Hikishima & Omura, 2012). Recent results from the TRISTAN-MP full-particle PIC code have also shown the frequent presence of simultaneous chorus waves generated with a significant frequency difference in simulations with a high initial anisotropy of the hot electron distribution (Kuzichev et al., 2019). The simultaneous presence of different waves has also been noticed in a Bayesian analysis of an observed long rising tone chorus element (Crabtree et al., 2017). Statistics of fast frequency variations inside chorus packets measured by the Van Allen Probes, as well as spectra of long wave packets, similarly suggest a frequent presence of wave superposition (X. J. Zhang, Mourenas, et al., 2020). Accordingly, the shortest wave packets in the electron hybrid simulation could have been partly formed by wave superposition, together with some amplitude modulation at the trapping frequency.

The larger median $\partial f/\partial t$ values in the electron hybrid simulation than in Van Allen Probes observations in Figure 6a could stem (a) from the roughly twice higher wave frequency in the simulation at $L = 4$ than in statistical observations at $L \sim 5$, or (b) from a superposition of three waves instead of two, or (c) from the roughly twice larger peak amplitude of wave packets in the simulation than in observations (see Figure 6b). To check the effect of wave frequency, Figures 6c and 6d show the distribution of wave packets in the $(\beta, |\partial f/\partial t|/f^2)$ space for the four different codes and for satellite observations, using the normalized sweep rate $|\partial f/\partial t|/f^2$ independent of wave frequency. Wave packets from all simulations are now shifted well inside the main region of chorus wave packet observations (in red and yellow). Both simulations and observations clearly show the same physical trend $|\partial f/\partial t| \sim (0.5-1) \times f^2/\beta^2$, in agreement with the suggested mechanisms of wave superposition or nonlinear amplitude modulation and frequency drift. Further investigations have started to assess the relative importance of these two mechanisms in observations and simulations (Nunn et al., 2021). But this is beyond the scope of the present paper and it is left for future work.

5. Conclusions

In the present paper, we have compared the fine structure of waves produced by four different codes of nonlinear chorus wave generation with statistical results from the Van Allen Probes in the inner magnetosphere. We used the same method of wave packet identification and analysis for all these datasets, focusing on the near equatorial source region where chorus waves are generated. Simulations performed with the backward-wave-oscillator code, electron hybrid code, Vlasov hybrid code, and DAWN hybrid code, have all produced wave packets having very similar characteristics as the observed chorus wave packets. The four simulations have recovered different, and remarkably complementary, parameter domains of observed wave packet sizes, amplitudes, and frequency sweep rates. This demonstrates the reliability of these different codes in reproducing realistic chorus waves observed by satellites in the outer radiation belt and in the plasma sheet. These four codes can therefore be used with confidence to study chorus wave generation, and to better understand and predict the dynamics of electrons interacting with these waves.

In all simulations, wave packet sizes and amplitudes were found to increase with propagation away from the equator, as expected for a nonlinear convective wave growth from the equatorial source region (Omura et al., 2008; Summers et al., 2012). In addition, all simulations allowed to produce at least some short wave packets (10 wave periods long or less) with large frequency sweep rates, with relatively similar amounts of rising and falling frequency short packets, as for the overwhelming majority of the observed chorus wave packets. This result was obtained in spite of the mainly rising tone appearance of individual chorus waves over much longer times scales ($> 0.05-0.1$ s) in simulations and observations. The two main physical trends of wave packet size increase like $\beta \sim B_{w,peak}^{3/2}$ and frequency sweep rate variation like $|\partial f/\partial t| \sim f^2/\beta^2$ identified in statistical observations from the Van Allen Probes were fairly well reproduced in the simulations. These characteristics of short wave packets (or subpackets) are probably related to nonlinear trapping-induced amplitude modulation and frequency drift (Demekhov & Trakhtengerts, 2008; Omura et al., 2008; Tao et al., 2017; Trakhtengerts et al., 2004) and/or to the presence of wave superposition (Nunn et al., 2021; X. J. Zhang, Mourenas, et al., 2020), identified in some simulations.

However, it is worth emphasizing the wide parameter domain (of packet sizes, amplitudes, and frequency sweep rates) of chorus wave packets measured by satellites. The different initial conditions used in each

simulation (plasma density, electron gyrofrequency, wave frequency, anisotropy of the energetic electron distribution) have been found to often lead to different wave packet sizes, amplitudes, and sweep rates. Therefore, great care should be exerted when selecting initial conditions in a given code to reproduce a particular parameter domain of the observed chorus waves - for example, the more frequent moderate amplitude short packets, or the less frequent but more intense long wave packets (X. Zhang et al., 2019). In the future, it would be interesting to perform a similar comparison between the fine structure of oblique chorus waves in observations and in numerical simulations, since the nonlinear evolution of intense oblique waves is probably quite complex (Agapitov, Drake, et al., 2018).

Data Availability Statement

Van Allen Probes EMFISIS data were obtained from https://emfisis.physics.uiowa.edu/data/index, and THEMIS data from http://themis.ssl.berkeley.edu/. Data access and processing were done using SPEDAS V3.1 (Angelopoulos et al., 2019).

Acknowledgments
The work of X.-J. Zhang and A. V. Artemyev was supported by the NSF grants 2021749, 2026375, and NASA grant 80NSSC20K1578. A. Demekhov was supported by the Russian Science Foundation under grant no. 21-12-00416. Y. Katoh was supported by Grants-in-Aid for Scientific Research (15H05747, 18H03727, 20H01959, and 20K04052) and Y. Omura was supported by 17H06140 of Japan Society for the Promotion of Science. X.-J. Zhang, A. V. Artemyev, and V. Artemyev acknowledge NASA contract NAS5-02099 for use of data from the THEMIS Mission, specifically J. W. Bonnell and F. S. Mozer for use of EFI data, O. LeContel and the late A. Roux for use of SCM data, and K. H. Glassmeier, U. Auster and W. Baumjohann for use of FGM data provided under the lead of the Technical University of Braunschweig and with financial support through the German Ministry for Economy and Technology and the German Center for Aviation and Space under contract 50 OC 0302.

References

Agapitov, O. V., Artemyev, A., Krasnoselskikh, V., Khotyaintsev, Y. V., Mourenas, D., Breuillard, H., & Rolland, G. (2013). Statistics of whistler mode waves in the outer radiation belt: Cluster STAFF-SA measurements. *Journal of Geophysical Research*, *118*, 3407–3420. https://doi.org/10.1002/jgra.50312

Agapitov, O. V., Drake, J. F., Vasko, I., Mozer, F. S., Artemyev, A., Krasnoselskikh, V., & Reeves, G. D. (2018). Nonlinear electrostatic steepening of whistler waves: The guiding factors and dynamics in inhomogeneous systems. *Geophysical Research Letters*, *45*, 2168–2176. https://doi.org/10.1002/2017GL076957

Agapitov, O. V., Mourenas, D., Artemyev, A. V., Mozer, F. S., Hospodarsky, G., Bonnell, J., & Krasnoselskikh, V. (2018). Synthetic empirical chorus wave model from combined Van Allen Probes and cluster statistics. *Journal of Geophysical Research: Space Physics*, *123*(1), 297–314. https://doi.org/10.1002/2017JA024843

Albert, J. M. (2002). Nonlinear interaction of outer zone electrons with VLF waves. *Geophysical Research Letters*, *29*, 1275–1281. https://doi.org/10.1029/2001GL013941

Angelopoulos, V. (2008). The THEMIS mission. *Space Science Reviews*, *141*, 5–34. https://doi.org/10.1007/s11214-008-9336-1

Angelopoulos, V., Cruce, P., Drozdov, A., Grimes, E. W., Hatzigeorgiu, N., King, D. A., & Schroeder, P. (2019). The space physics environment data analysis system (SPEDAS). *Space Science Reviews*, *215*, 9. https://doi.org/10.1007/s11214-018-0576-4

Artemyev, A. V., Vasiliev, A. A., Mourenas, D., Agapitov, O. V., & Krasnoselskikh, V. V. (2014). Electron scattering and nonlinear trapping by oblique whistler waves: The critical wave intensity for nonlinear effects. *Physics of Plasmas*, *21*(10), 102903. https://doi.org/10.1063/1.4897945

Auster, H. U., Glassmeier, K. H., Magnes, W., Aydogar, O., Baumjohann, W., Constantinescu, D., & Wiedemann, M. (2008). The THEMIS fluxgate magnetometer. *Space Science Reviews*, *141*, 235–264. https://doi.org/10.1007/s11214-008-9365-9

Bonnell, J. W., Mozer, F. S., Delory, G. T., Hull, A. J., Ergun, R. E., Cully, C. M., & Harvey, P. R. (2008). The electric field instrument (EFI) for THEMIS. *Space Science Reviews*, *141*, 303–341. https://doi.org/10.1007/s11214-008-9469-2

Burtis, W. J., & Helliwell, R. A. (1976). Magnetospheric chorus - Occurrence patterns and normalized frequency. *Planetary Space Science*, *24*, 1007–1024. https://doi.org/10.1016/0032-0633(76)90119-7

Cattell, C., Wygant, J. R., Goetz, K., Kersten, K., Kellogg, P. J., von Rosenvinge, T., & Russell, C. T. (2008). Discovery of very large amplitude whistler-mode waves in Earth's radiation belts. *Geophysical Research Letters*, *35*, 1105. https://doi.org/10.1029/2007GL032009

Chen, L., Breneman, A. W., Xia, Z., & Zhang, X.-J. (2020). Modeling of bouncing electron microbursts induced by ducted chorus waves. *Geophysical Research Letters*, *47*(17), e89400. https://doi.org/10.1029/2020GL089400

Crabtree, C., Tejero, E., Ganguli, G., Hospodarsky, G. B., & Kletzing, C. A. (2017). Bayesian spectral analysis of chorus subelements from the Van Allen Probes. *Journal of Geophysical Research: Space Physics*, *122*(6), 6088–6106. https://doi.org/10.1002/2016JA023547

Cully, C. M., Angelopoulos, V., Auster, U., Bonnell, J., & Le Contel, O. (2011). Observational evidence of the generation mechanism for rising-tone chorus. *Geophysical Research Letters*, *38*, 1106. https://doi.org/10.1029/2010GL045793

Demekhov, A. G. (2011). Generation of VLF emissions with the increasing and decreasing frequency in the magnetospheric cyclotron maser in the backward wave oscillator regime. *Radiophysics and Quantum Electronics*, *53*, 609–622. https://doi.org/10.1007/s11141-011-9256-x

Demekhov, A. G., Taubenschuss, U., & Santolík, O. (2017). Simulation of VLF chorus emissions in the magnetosphere and comparison with THEMIS spacecraft data. *Journal of Geophysical Research*, *122*, 166–184. https://doi.org/10.1002/2016JA023057

Demekhov, A. G., & Trakhtengerts, V. Y. (2008). Dynamics of the magnetospheric cyclotron ELF/VLF maser in the backward-wave-oscillator regime. II. The influence of the magnetic-field inhomogeneity. *Radiophysics and Quantum Electronics*, *51*, 880–889. https://doi.org/10.1007/s11141-009-9093-3

Demekhov, A. G., Trakhtengerts, V. Y., Rycroft, M., & Nunn, D. (2009). Efficiency of electron acceleration in the Earth's magnetosphere by whistler mode waves. *Geomagnetism and Aeronomy*, *49*, 24–29. https://doi.org/10.1134/S0016793209010034

Hikishima, M., & Omura, Y. (2012). Particle simulations of whistler-mode rising-tone emissions triggered by waves with different amplitudes. *Journal of Geophysical Research*, *117*, A04226. https://doi.org/10.1029/2011JA017428

Karpman, V. I., Istomin, J. N., & Shklyar, D. R. (1974). Nonlinear theory of a quasi-monochromatic whistler mode packet in inhomogeneous plasma. *Plasma Physics*, *16*, 685–703. https://doi.org/10.1088/0032-1028/16/8/001

Katoh, Y., & Omura, Y. (2004). Acceleration of relativistic electrons due to resonant scattering by whistler mode waves generated by temperature anisotropy in the inner magnetosphere. *Journal of Geophysical Research*, *109*, 12214. https://doi.org/10.1029/2004JA010654

Katoh, Y., & Omura, Y. (2007). Computer simulation of chorus wave generation in the Earth's inner magnetosphere. *Geophysical Research Letters*, *34*, 3102. https://doi.org/10.1029/2006GL028594

Katoh, Y., & Omura, Y. (2013). Effect of the background magnetic field inhomogeneity on generation processes of whistler-mode chorus and broadband hiss-like emissions. *Journal of Geophysical Research*, *118*, 4189–4198. https://doi.org/10.1002/jgra.50395

Katoh, Y., & Omura, Y. (2016). Electron hybrid code simulation of whistler-mode chorus generation with real parameters in the Earth's inner magnetosphere. *Earth Planets and Space*, *68*(1), 192. https://doi.org/10.1186/s40623-016-0568-0

Kletzing, C. A., Kurth, W. S., Acuna, M., MacDowall, R. J., Torbert, R. B., Averkamp, T., & Tyler, J. (2013). The electric and magnetic field instrument suite and integrated science (EMFISIS) on RBSP. *Space Science Reviews*, *179*, 127–181. https://doi.org/10.1007/s11214-013-9993-6

Kubota, Y., & Omura, Y. (2018). Nonlinear dynamics of radiation belt electrons interacting with chorus emissions localized in longitude. *Journal of Geophysical Research: Space Physics*, *123*, 4835–4857. https://doi.org/10.1029/2017JA025050

Kurth, W. S., De Pascuale, S., Faden, J. B., Kletzing, C. A., Hospodarsky, G. B., Thaller, S., & Wygant, J. R. (2015). Electron densities inferred from plasma wave spectra obtained by the Waves instrument on Van Allen Probes. *Journal of Geophysical Research: Space Physics*, *120*, 904–914. https://doi.org/10.1002/2014JA020857

Kuzichev, I. V., Soto-Chavez, A. R., Park, J., Gerrard, A., & Spitkovsky, A. (2019). Magnetospheric chorus wave simulation with the TRISTAN-MP PIC code. *Physics of Plasmas*, *26*(7), 072901. https://doi.org/10.1063/1.5096537

Le Contel, O., Roux, A., Robert, P., Coillot, C., Bouabdellah, A., de La Porte, B., & Larson, D. (2008). First results of the themis search coil magnetometers. *Space Science Reviews*, *141*, 509–534. https://doi.org/10.1007/s11214-008-9371-y

LeDocq, M. J., Gurnett, D. A., & Hospodarsky, G. B. (1998). Chorus source locations from VLF Poynting flux measurements with the polar spacecraft. *Geophysical Research Letters*, *25*, 4063–4066. https://doi.org/10.1029/1998GL900071

Li, W., Bortnik, J., Thorne, R. M., & Angelopoulos, V. (2011). Global distribution of wave amplitudes and wave normal angles of chorus waves using THEMIS wave observations. *Journal of Geophysical Research*, *116*, 12205. https://doi.org/10.1029/2011JA017035

Li, W., Bortnik, J., Thorne, R. M., Cully, C. M., Chen, L., Angelopoulos, V., & Lecontel, O. (2013). Characteristics of the Poynting flux and wave normal vectors of whistler-mode waves observed on THEMIS. *Journal of Geophysical Research: Space Physics*, *118*, 1461–1471. https://doi.org/10.1002/jgra.50176

Li, W., Thorne, R. M., Bortnik, J., Shprits, Y. Y., Nishimura, Y., Angelopoulos, V., & Bonnell, J. W. (2011). Typical properties of rising and falling tone chorus waves. *Geophysical Research Letters*, *38*, 14103. https://doi.org/10.1029/2011GL047925

Lu, Q., Ke, Y., Wang, X., Liu, K., Gao, X., Chen, L., & Wang, S. (2019). Two-dimensional gcPIC simulation of rising-tone chorus waves in a dipole magnetic field. *Journal of Geophysical Research: Space Physics*, *124*(6), 4157–4167. https://doi.org/10.1029/2019JA026586

Macúšová, E., SantolíK, O., DécréAu, P., Demekhov, A. G., Nunn, D., Gurnett, D. A., et al. (2010). Observations of the relationship between frequency sweep rates of chorus wave packets and plasma density. *Journal of Geophysical Research*, *115*(A12), A12257. https://doi.org/10.1029/2010JA015468

Mauk, B. H., Fox, N. J., Kanekal, S. G., Kessel, R. L., Sibeck, D. G., & Ukhorskiy, A. (2013). Science objectives and rationale for the Radiation Belt Storm Probes mission. *Space Science Reviews*, *179*, 3–27. https://doi.org/10.1007/s11214-012-9908-y

Meredith, N. P., Horne, R. B., & Anderson, R. R. (2001). Substorm dependence of chorus amplitudes: Implications for the acceleration of electrons to relativistic energies. *Journal of Geophysical Research*, *106*, 13165–13178. https://doi.org/10.1029/2000JA900156

Miyoshi, Y., Saito, S., Seki, K., Nishiyama, T., Kataoka, R., Asamura, K., & Santolik, O. (2015). Relation between fine structure of energy spectra for pulsating aurora electrons and frequency spectra of whistler mode chorus waves. *Journal of Geophysical Research: Space Physics*, *120*, 7728–7736. https://doi.org/10.1002/2015JA021562

Morales, G., & O'Neil, T. (1972). Nonlinear frequency shift of an electron plasma wave. *Physical Review Letters*, *28*, 417–420. https://doi.org/10.1103/PhysRevLett.28.417

Mourenas, D., Zhang, X.-J., Artemyev, A. V., Angelopoulos, V., Thorne, R. M., Bortnik, J., & Vasiliev, A. A. (2018). Electron nonlinear resonant interaction with short and intense parallel chorus wave packets. *Journal of Geophysical Research: Space Physics*, *123*, 4979–4999. https://doi.org/10.1029/2018JA025417

Nunn, D. (1974). A self-consistent theory of triggered VLF emissions. *Planetary Space Science*, *22*, 349–378. https://doi.org/10.1016/0032-0633(74)90070-1

Nunn, D. (1986). A nonlinear theory of sideband stability in ducted whistler mode waves. *Planetary Space Science*, *34*, 429–451. https://doi.org/10.1016/0032-0633(86)90032-2

Nunn, D., & Omura, Y. (2012). A computational and theoretical analysis of falling frequency VLF emissions. *Journal of Geophysical Research*, *117*, 8228. https://doi.org/10.1029/2012JA017557

Nunn, D., Rycroft, M., & Trakhtengerts, V. (2005). A parametric study of the numerical simulations of triggered VLF emissions. *Annales Geophysicae*, *23*(12), 3655–3666. https://doi.org/10.5194/angeo-23-3655-2005

Nunn, D., Santolik, O., Rycroft, M., & Trakhtengerts, V. (2009). On the numerical modelling of VLF chorus dynamical spectra. *Annales Geophysicae*, *27*, 2341–2359. https://doi.org/10.5194/angeo-27-2341-2009

Nunn, D., Zhang, X.-J., Mourenas, D., & Artemyev, A. V. (2021). Generation of realistic short chorus wave packets. *Geophysical Research Letters*, *48*, e2020GL092178. https://doi.org/10.1029/2020GL092178

Omura, Y., Katoh, Y., & Summers, D. (2008). Theory and simulation of the generation of whistler-mode chorus. *Journal of Geophysical Research*, *113*, 4223. https://doi.org/10.1029/2007JA012622

Omura, Y., Nunn, D., & Summers, D. (2013). Generation processes of whistler mode chorus emissions: Current status of nonlinear wave growth theory. In D. Summers, I. U. Mann, D. N. Baker, & M. Schulz (Eds.), *Dynamics of the Earth's radiation belts and inner magnetosphere* (pp. 243–254). https://doi.org/10.1029/2012GM001347

Saito, S., Miyoshi, Y., & Seki, K. (2012). Relativistic electron microbursts associated with whistler chorus rising tone elements: GEMSIS-RBW simulations. *Journal of Geophysical Research*, *117*, A10206. https://doi.org/10.1029/2012JA018020

Santolík, O., Gurnett, D., & Pickett, J. (2004). Multipoint investigation of the source region of storm-time chorus. *Annales Geophysicae*, *22*(7), 2555–2563. https://doi.org/10.5194/angeo-22-2555-2004

Santolík, O., Gurnett, D. A., Pickett, J. S., Parrot, M., & Cornilleau-Wehrlin, N. (2003). Spatio-temporal structure of storm-time chorus. *Journal of Geophysical Research*, *108*, 1278. https://doi.org/10.1029/2002JA009791

Santolík, O., Kletzing, C. A., Kurth, W. S., Hospodarsky, G. B., & Bounds, S. R. (2014). Fine structure of large-amplitude chorus wave packets. *Geophysical Research Letters*, *41*, 293–299. https://doi.org/10.1002/2013GL058889

Santolík, O., Macúšová, E., Kolmašová, I., Cornilleau-Wehrlin, N., & Conchy, Y. (2014). Propagation of lower-band whistler-mode waves in the outer Van Allen belt: Systematic analysis of 11 years of multi-component data from the Cluster spacecraft. *Geophysical Research Letters*, *41*, 2729–2737. https://doi.org/10.1002/2014GL059815

Shklyar, D. R., & Matsumoto, H. (2009). Oblique whistler-mode waves in the inhomogeneous magnetospheric plasma: Resonant interactions with energetic charged particles. *Surveys in Geophysics*, *30*, 55–104. https://doi.org/10.1007/s10712-009-9061-7

Summers, D., Omura, Y., Miyashita, Y., & Lee, D.-H. (2012). Nonlinear spatiotemporal evolution of whistler mode chorus waves in Earth's inner magnetosphere. *Journal of Geophysical Research*, *117*, 9206. https://doi.org/10.1029/2012JA017842

Summers, D., Tang, R., Omura, Y., & Lee, D.-H. (2013). Parameter spaces for linear and nonlinear whistler-mode waves. *Physics of Plasmas*, *20*(7), 072110. https://doi.org/10.1063/1.4816022

Tao, X. (2014). A numerical study of chorus generation and the related variation of wave intensity using the DAWN code. *Journal of Geophysical Research: Space Physics*, *119*(5), 3362–3372. https://doi.org/10.1002/2014JA019820

Tao, X., Bortnik, J., Albert, J. M., Thorne, R. M., & Li, W. (2013). The importance of amplitude modulation in nonlinear interactions between electrons and large amplitude whistler waves. *Journal of Atmospheric and Solar-Terrestrial Physics*, *99*, 67–72. https://doi.org/10.1016/j.jastp.2012.05.012

Tao, X., Li, W., Bortnik, J., Thorne, R. M., & Angelopoulos, V. (2012). Comparison between theory and observation of the frequency sweep rates of equatorial rising tone chorus. *Geophysical Research Letters*, *39*(8), L08106. https://doi.org/10.1029/2012GL051413

Tao, X., Lu, Q., Wang, S., & Dai, L. (2014). Effects of magnetic field configuration on the day-night asymmetry of chorus occurrence rate: A numerical study. *Geophysical Research Letters*, *41*, 6577–6582. https://doi.org/10.1002/2014GL061493

Tao, X., Zonca, F., & Chen, L. (2017). Identify the nonlinear wave-particle interaction regime in rising tone chorus generation. *Geophysical Research Letters*, *44*(8), 3441–3446. https://doi.org/10.1002/2017GL072624

Tao, X., Zonca, F., Chen, L., & Wu, Y. (2020). Theoretical and numerical studies of chorus waves: A review. *Science China Earth Sciences*, *63*(1), 78–92. https://doi.org/10.1007/s11430-019-9384-6

Taubenschuss, U., Khotyaintsev, Y. V., Santolík, O., Vaivads, A., Cully, C. M., Contel, O. L., & Angelopoulos, V. (2014). Wave normal angles of whistler mode chorus rising and falling tones. *Journal of Geophysical Research: Space Physics*, *119*, 9567–9578. https://doi.org/10.1002/2014JA020575

Trakhtengerts, V. Y., Demekhov, A. G., Titova, E. E., Kozelov, B. V., Santolik, O., Gurnett, D., & Parrot, M. (2004). Interpretation of cluster data on chorus emissions using the backward wave oscillator model. *Physics of Plasmas*, *11*, 1345–1351. https://doi.org/10.1063/1.1667495

Tsurutani, B. T., & Smith, E. J. (1974). Postmidnight chorus: A substorm phenomenon. *Journal of Geophysical Research*, *79*, 118–127. https://doi.org/10.1029/JA079i001p00118

Vainchtein, D., Zhang, X.-J., Artemyev, A., Mourenas, D., Angelopoulos, V., & Thorne, R. M. (2018). Evolution of electron distribution driven by nonlinear resonances with intense field-aligned chorus waves. *Journal of Geophysical Research: Space Physics*, *123*, 8149–8169. https://doi.org/10.1029/2018ja025654

Vomvoridis, J. L., Crystal, T. L., & Denavit, J. (1982). Theory and computer simulations of magnetospheric very low frequency emissions. *Journal of Geophysical Research*, *87*, 1473–1489. https://doi.org/10.1029/JA087iA03p01473

Wilson, L. B., III, Cattell, C. A., Kellogg, P. J., Wygant, J. R., Goetz, K., Breneman, A., & Kersten, K. (2011). The properties of large amplitude whistler mode waves in the magnetosphere: Propagation and relationship with geomagnetic activity. *Geophysical Research Letters*, *38*, 17107. https://doi.org/10.1029/2011GL048671

Wu, Y., Tao, X., Zonca, F., Chen, L., & Wang, S. (2020). Controlling the chirping of chorus waves via magnetic field inhomogeneity. *Geophysical Research Letters*, *47*(10), e87791. https://doi.org/10.1029/2020GL087791

Yamaguchi, K., Matsumuro, T., Omura, Y., & Nunn, D. (2013). Ray tracing of whistler-mode chorus elements: Implications for generation mechanisms of rising and falling tone emissions. *Annales Geophysicae*, *31*, 665–673. https://doi.org/10.5194/angeo-31-665-2013

Zhang, X., Angelopoulos, V., Artemyev, A. V., & Liu, J. (2019). Energy transport by whistler waves around dipolarizing flux bundles. *Geophysical Research Letters*, *46*(21), 718–11727. https://doi.org/10.1029/2019GL084226

Zhang, X. J., Agapitov, O., Artemyev, A. V., Mourenas, D., Angelopoulos, V., Kurth, W. S., & Hospodarsky, G. B. (2020). Phase decoherence within intense chorus wave packets constrains the efficiency of nonlinear resonant electron acceleration. *Geophysical Research Letters*, *47*(20), e89807. https://doi.org/10.1029/2020GL089807

Zhang, X. J., Mourenas, D., Artemyev, A. V., Angelopoulos, V., Bortnik, J., Thorne, R. M., & Hospodarsky, G. B. (2019). Nonlinear Electron interaction with intense chorus waves: Statistics of occurrence rates. *Geophysical Research Letters*, *46*(13), 7182–7190. https://doi.org/10.1029/2019GL083833

Zhang, X. J., Mourenas, D., Artemyev, A. V., Angelopoulos, V., Kurth, W. S., Kletzing, C. A., & Hospodarsky, G. B. (2020). Rapid frequency variations within intense chorus wave packets. *Geophysical Research Letters*, *47*(15), e88853. https://doi.org/10.1029/2020GL088853

Zhang, X. J., Thorne, R., Artemyev, A., Mourenas, D., Angelopoulos, V., Bortnik, J., & Hospodarsky, G. B. (2018). Properties of intense field-aligned lower-band chorus waves: Implications for nonlinear wave-particle interactions. *Journal of Geophysical Research: Space Physics*, *123*(7), 5379–5393. https://doi.org/10.1029/2018JA025390